The influence of regular surface patterns on cloud cavitation about a hydrofoil

IOP Conf. Series: Earth and Environmental Science **1561** (2025) 012009 doi:10.1088/1755-1315/1561/1/012009

The influence of regular surface patterns on cloud cavitation about a hydrofoil

Timon Krimm[1], Grigorios Hatzissawidis[1], Gerhard Ludwig[1], Maximilian Kuhr[1] and Peter Pelz[1]

[1]Chair of Fluid Systems, Technische Universität Darmstadt, Otto-Berndt-Str. 2, 64287 Darmstadt, Germany

E-mail: timon.krimm@tu-darmstadt.de

Abstract. Two hydrofoils with different obstacle configurations were examined in the cavitation tunnel at Technische Universität Darmstadt to quantify the influence of the obstacles on cavitation dynamics. Both the cavitation number and the incidence were varied. High-speed imaging and high-frequency pressure measurements were conducted to identify characteristic time scales (shedding frequency) and length scales (cavity sheet length). The power spectral density (PSD) of the pressure data was estimated to isolate the characteristic shedding frequencies of cloud cavitation. The examination of the cavitation topology and spectra enables the separation between (i) condensation shockwave and (ii) re-entrant flow as dominant cloud shedding mechanism. The influence of the obstacles is primarily visible in a reduction of shedding frequencies correlated to the re-entrant flow. In addition, there is an effect on the frequencies associated with shockwave-driven cloud cavitation, which could be related to the hindrance of the re-entrant flow. The cavity sheet was automatically detected using a convolutional neural network (CNN). Two methods were applied to obtain the average and maximum cavity sheet length. As expected, the extent of the cavity sheet increases as the cavitation number is reduced. The influence of the obstacles on the cavity sheet length is only apparent if an obstacle is located close to the leading edge.

1 Introduction

Cloud cavitation is known to be the most severe type of hydrodynamic cavitation, which is reflected in an increase in noise and erosive potential [1, 2, 3]. The appearance of cloud cavitation is characterised by the periodic shedding of large-scale structures ('clouds') from the cavity sheet, followed by their collapse. There are two main mechanisms that can be responsible for the development of cloud cavitation. The re-entrant flow is a liquid film that moves upstream beneath the cavity sheet and eventually cuts it off [4]. In case of shockwave-driven cloud cavitation the cavity sheet is shed by a bubbly shock that propagates through the cavity until it reaches its beginning [5]. These shedding mechanisms can be separated by visual appearance, as well as by their shedding frequencies. Smith et al. [6] showed that the shedding frequency that corresponds to shockwave-driven cloud cavitation is independent of the cavitation number σ, while the shedding frequencies caused by the re-entrant flow are highly dependent on σ. It can also be seen from a spectrogram that shockwave-driven cloud cavitation generally occurs at lower cavitation numbers and that there is a transition region in which both mechanisms occur simultaneously [6, 7].

Numerous studies are conducted regarding the control of cloud cavitation by stopping the re-entrant flow using obstacles. Kawanami et al. [8] investigated different obstacle configurations on an elliptic nose hydrofoil using a bar with a square cross-sectional area. The height of the bar was 1.3 % of the chord

length L_c. They found that the bar could prevent cloud cavitation and reduce cavitation noise by 40 % when placed at a position which was reached by the extent of the cavitation sheet without obstacles. As soon as the obstacle was placed downstream of the maximum sheet length, no effect was visible. This blockage effect of the re-entrant flow was confirmed by other researchers [9, 10, 11]. Zhang et al. [10] and Che et al. [11] also found a reduction of the cavity sheet length when an obstacle was applied. Ganesh [12] investigated the influence of an obstacle on shockwave-driven cloud cavitation and found that the obstacle has no effect on the shedding dynamics. The results reported by Sato et al. [9] and Che et al. [11] led to the same conclusion as they found that cavitation could not be suppressed in their experiments for transitional cavity oscillation conditions.

In this paper, the influence of a single obstacle as well as multiple obstacles on cloud cavitation is determined. High-frequency pressure measurements are carried out to identify the effect on the shedding frequencies of the different cloud shedding mechanisms and the transitional area between them. Spectrograms of the different configurations are compared with the reference configuration without obstacles. High-speed photographs are analysed using a convolutional neural network (CNN) to identify the cavity sheet length.

2 Experimental setup

The experiments were carried out in the cavitation tunnel at the Chair of Fluid Systems at TU Darmstadt. The test section has a cross-sectional area of 25 mm × 70 mm and is visually accessible from three sides thanks to the use of acrylic glass panes. The velocity in the test section can be set up to a maximum of 30 m/s. A system pressure regulation up to 10 bar enables the adjustment of the cavitation number. The hydrofoil is placed inside the test section using a rotatable specimen holder. It allows to adjust the incidence angle α with an uncertainty of $\pm 0.1°$. For a detailed description of the cavitation tunnel the authors refer to [13].

Three hydrofoil configurations are investigated. They differ in the number and position of the applied obstacles. The base is a hydraulically smooth, circular leading edge (CLE) hydrofoil. It has a chord length of $L = 40$ mm, a thickness of 6 mm and a span of 25 mm. The obstacles which are used have a cross section of 0.3 mm × 0.5 mm, as shown in detail A in figure 1, and cover the whole span. In the first configuration (I) a single obstacle is placed at $x = 0.3\,L$. A drawing of the cross section of this hydrofoil is shown in figure 1. In the second configuration (II), seven obstacles are placed on the hydrofoil. The distance between the leading edge of the hydrofoil and the leading edge of the first obstacle is 3 mm, as is the centre distance between the obstacles. Apart from the position and number of obstacles, all hydrofoils have the same dimensions.

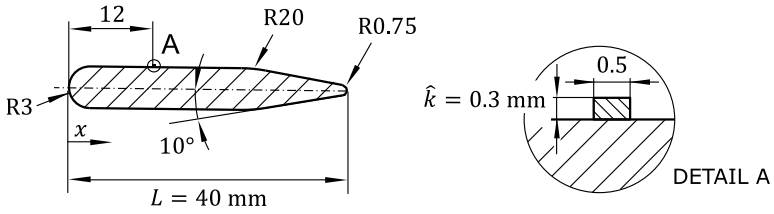

Figure 1: Drawing of the cross-section of the CLE hydrofoil with dimensions and position of the obstacle for the first examined configuration (I).

The experimental design consists of 53 operating points for each hydrofoil. An operating point is defined by the Reynolds number, the incidence and the cavitation number. The Reynolds number $Re := UL/\nu$ is calculated with the free-stream velocity in the test section U and the kinematic viscosity ν of water based on the current temperature. The temperature was set to 23.5 ± 0.5 °C via an external cooling circuit. This temperature was also used for the determination of the density ϱ and the vapour pressure p_v for the calculation of the cavitation number $\sigma := 2(p - p_v)/\varrho U$. Here, p is the static pressure in the test section 143 mm upstream the centre of the hydrofoil. The Reynolds number was fixed at 1.2×10^6, while two incidence angles $\alpha = 2°$ and $4°$ were examined. The cavitation number was varied to cover the regimes from sheet cavitation to supercavitation. This resulted in a range from $\sigma = 0.7$ to 1.8 and $\sigma = 0.7$ to 2.0 for the respective incidence angle, with an increment size of $\Delta\sigma = 0.5$.

The sound pressure measurements were conducted using a hydrophone by Bruel&Kjaer (Type 8103). It was mounted in an acrylic side pane of the test section 64 mm downstream the centre of the hydrofoil with an offset of approximately 9 mm above the cavitating surface. The signal was amplified by a

Bruel&Kjaer Type 2650 and recorded with a NI 9223 cDAQ module. The sampling rate was set to 200 kS/s with an acquisition time of 20 s. An IDT Y7-S3 high-speed camera was used for the high-speed imaging at a frame rate of 18 000 fps and a recording time of 1.25 s.

3 Methods

The frequency spectra of the sound pressure measurements are determined with Welch's method using a Hann window with a size of 200 000 samples and a 50 % overlap. The spectrograms are generated from the spectra for the specific σ by placing them next to each other. The contour plot enables a visual differentiation between the frequency domains that are characteristic for re-entrant flow and shockwave-driven cloud cavitation. The frequency f is described in its dimensionless form by the chord-based Strouhal number $St = fL/U$. To analyse the influence of the different obstacle configurations on the shedding mechanisms, a second contour plot was created showing the deviations in power for the respective frequency ranges. For this purpose, the spectrogram assigned to the reference hydrofoil without obstacles is subtracted from the spectrograms corresponding to the hydrofoils with obstacles.

The high-speed images are used for the determination of the sheet length $\hat{a}$. Therefore, several image processing steps were conducted. At the beginning, the position in pixels of the hydrofoil's edges are determined. This step is necessary for the calculation of the spatial resolution and the image is also cropped to the sides of the hydrofoil. In addition to the images with cavitation, background images were also recorded. These are subtracted from the main images to achieve a better image recognition. The identification of regions with cavitation is performed by a CNN, which has been trained in such a way that it enables automatic detection almost independently of the setup and lighting conditions. The output of the CNN is a binary image. In a final step, an edge detection algorithm is used to identify the extent of the cavity sheet as well as fully detached clouds.

Two methods are applied for the calculation of the average and maximum sheet length, based on the time series of the sheet extent. For the first method, all images are split into 10 sections of 2250 samples. A skewed normal distribution is fitted to each of these sections, and its maximum is determined. The value received could be described as a weighted mean of the sheet extent, as it tends towards higher probability densities. An example of this behaviour is shown in figure 2. If the sheet length is normally distributed, this weighted mean value is identical to the arithmetic mean value.

The second method to calculate the maximum cavity sheet length is applied for the periodic shedding. The peaks are identified in the time series of the cavity sheet length, associated with the start (trailing edge) and the end (leading edge) of each distinct cycle. On each of the cycles, a median filter is applied to account for outliers, and the maximum extent for each cycle is detected. From these values, a mean and a corresponding standard deviation are obtained, as seen in figure 6.

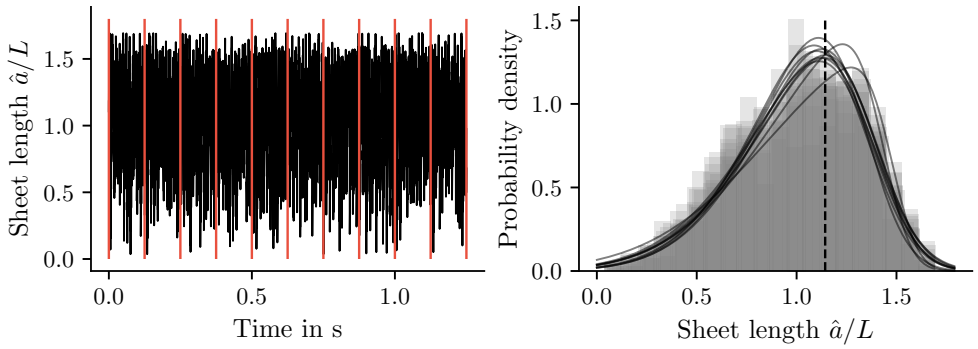

Figure 2: Illustration of the method used to determine the weighted mean sheet length.

4 Results and discussion

The spectrograms shown in figure 3 are obtained from the measurements with the base CLE hydrofoil for $\alpha = 2°$ (a) and 4° (b). Each spectrogram can be separated into four cavitation regimes. The first regime (i) is determined by shockwave-driven cloud cavitation. According to Smith et al. [6], the main shedding frequency and the higher harmonics appear as straight lines independent from the cavitation number for $St < 0.5$ and $St < 0.75$, respectively. In the second regime (ii) the re-entrant flow is the dominant cloud shedding mechanism. This can be recognised by the quadratic increase in the dominant frequency as

a function of the cavitation number. Between regime (i) and (ii), a small region where both shedding mechanisms appear simultaneously, is evident. As the cavitation number increases, larger clouds do not longer detach. This is denoted by the sheet cavitation regimes in figure 3.

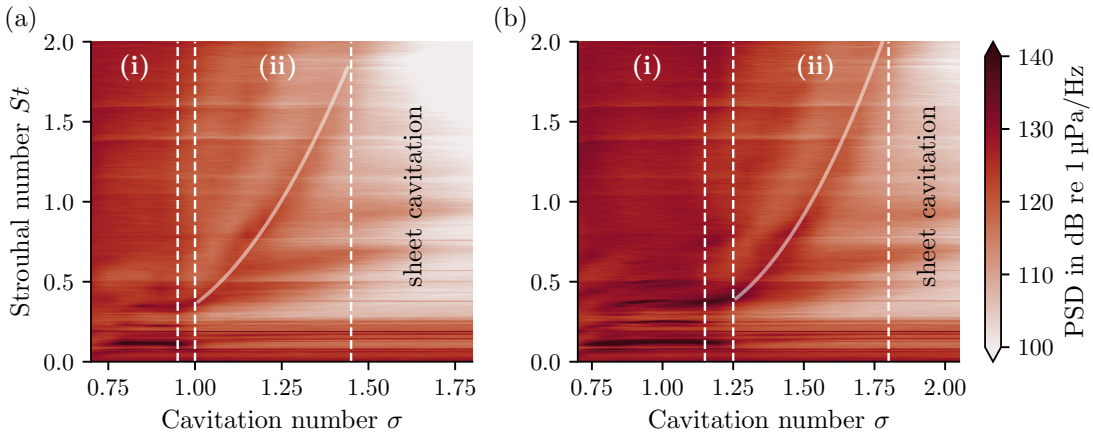

Figure 3: Spectrograms based on the hydrophone measurements for the hydrofoil without obstacles at $Re = 1.2 \times 10^6$ and $\alpha = 2°$ (a) or $\alpha = 4°$ (b). The numbered regimes correspond to shockwave-driven (i) and re-entrant flow-driven (ii) cloud cavitation.

Figure 4 displays spectrograms obtained from the PSD difference between the hydrofoil without obstacles and the hydrofoil with configuration (I) (a,b) or configuration (II) (c,d). The spectrograms on the left-hand side refer to an incidence of $\alpha = 2°$, while $\alpha = 4°$ applies to the spectrograms on the right-hand side. Looking at figure 4 (a,b), there is no change in the regime of shockwave-driven cloud cavitation (i). Thus, the single obstacle has no influence on the shockwave, which is consistent with the results from literature [12]. In regime (ii) there is a decrease in the energy of the frequencies that correspond to cloud shedding caused by the re-entrant flow, starting at $\sigma = 1.12$. For lower cavitation numbers there is no decrease visible. Re-entrant flow-driven cloud cavitation can be observed in the high-speed images for these operating points. It becomes clear that the single obstacle is only able to suppress the development or propagation of the re-entrant flow if the closure region is at a short distance downstream of the obstacle. Once the sheet extends further, the re-entrant flow is more developed when it reaches the obstacle and cannot be stopped, because of the insufficient obstacle height ($\hat{k}/L = 0.75\,\%$). For smaller sheet lengths, the fluid structure interaction with the obstacle leads to an increase in power of the frequencies $St > 1.5$ for $\sigma > 1.25$ and $\sigma > 1.5$ in figure 4 (a) and (b) respectively. In general, the qualitative effects of the obstacle on the frequency spectrum stay the same for $\alpha = 4°$, but the intensity decreases. This could be related to the increase of the cavity thickness for higher incidence.

As the number of obstacles increases, their influence becomes more recognisable, see figure 4 (c,d). At an incidence angle of $\alpha = 2°$, a significant change in the characteristic frequencies can be observed in regime (i). A distinction is made between two effects. At first, the lines corresponding to the main shedding frequency and its higher harmonics are shifted towards higher cavitation numbers. This shift is most likely caused by the first obstacle close to the leading edge of the hydrofoil. CFD simulation conducted by Z. Liu at RUB Bochum showed that the height of the obstacle is sufficient to influence the shear layer, which leads to an increase of the sheet length, as can be seen in figure 6(a). According to Hatzissawidis et al. [7], a discontinuous pressure distribution can initiate a shockwave leading to cloud shedding. The tapering of the CLE hydrofoil causes such a discontinuity. By extending the cavity sheet, the obstacle causes a transition between re-entrant flow and shockwave-driven cloud cavitation at higher cavitation numbers. The bigger sheet length also leads to an earlier formation of supercavitation, which results in a decrease in power of the frequencies $St < 0.5$ for $\sigma < 0.8$. The second influence of the obstacles in regime (i) is the slight shift to higher shedding frequencies ($\approx 5\,\mathrm{Hz}$), which is visible in figure 4 (c) in the form of the straight dark line above the bright line. This shift is caused by the absence of a second shedding cycle (245 Hz), which usually occurs within the main shockwave-driven shedding cycles in case of the hydrofoil without obstacles, as shown in figure 5. Since these cycles delay the development of the sheet, their absence leads to a slight increase in the dominant shedding frequency for the hydrofoils with

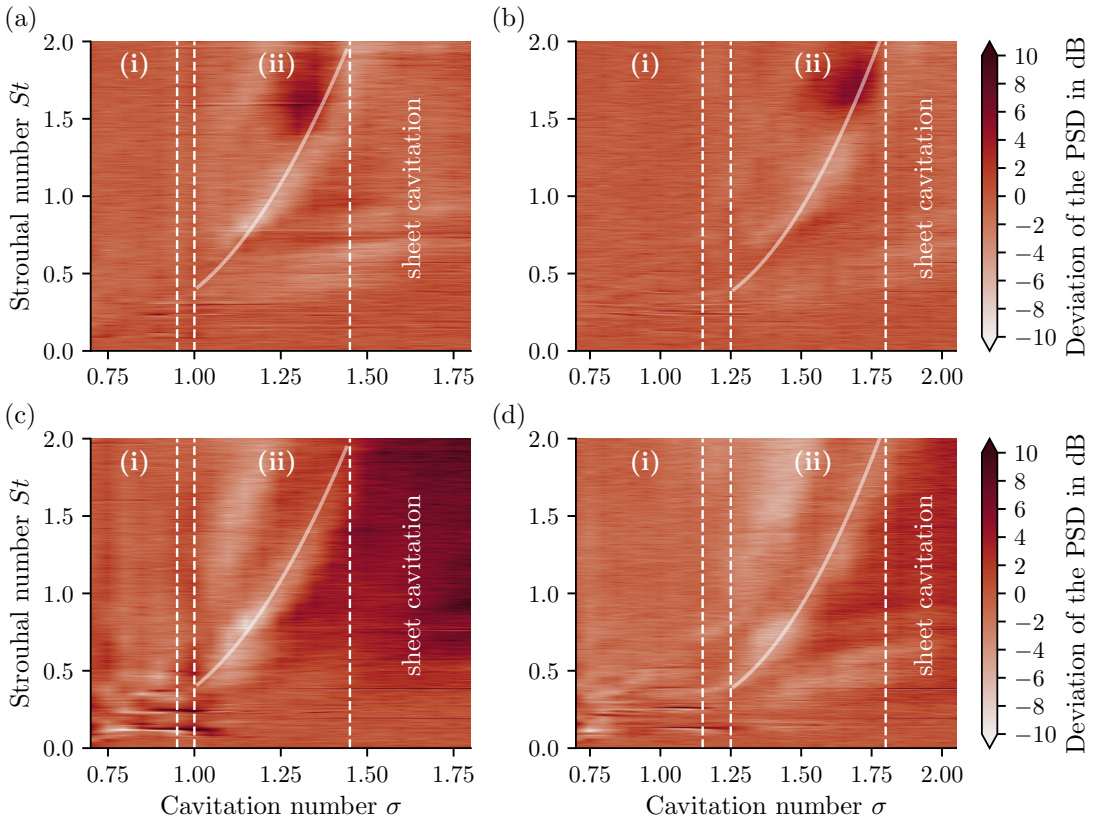

Figure 4: Spectrograms based on the deviations between the PSD of the hydrofoil without obstacles as reference and the hydrofoils with one obstacle at 0.3 L (a,b) or multiple obstacles (c,d). The measurements were conducted at $Re = 1.2 \times 10^6$ and $\alpha = 2°$ (a,c) or $\alpha = 4°$ (b,d). The numbered regimes correspond to shockwave-driven (i) and re-entrant flow-driven (ii) cloud cavitation.

obstacles. Visual assessment of the high-speed images does not allow for a clear conclusion regarding the underlying cause of the additional cycles. The shedding could be triggered by a re-entrant flow or a shockwave generated by the imploding cloud of the main cycle. In configuration (I), the additional cycles occur less frequently and decrease even further in configuration (II). This suggests that the re-entrant flow is the cause, as the obstacles could suppress it.

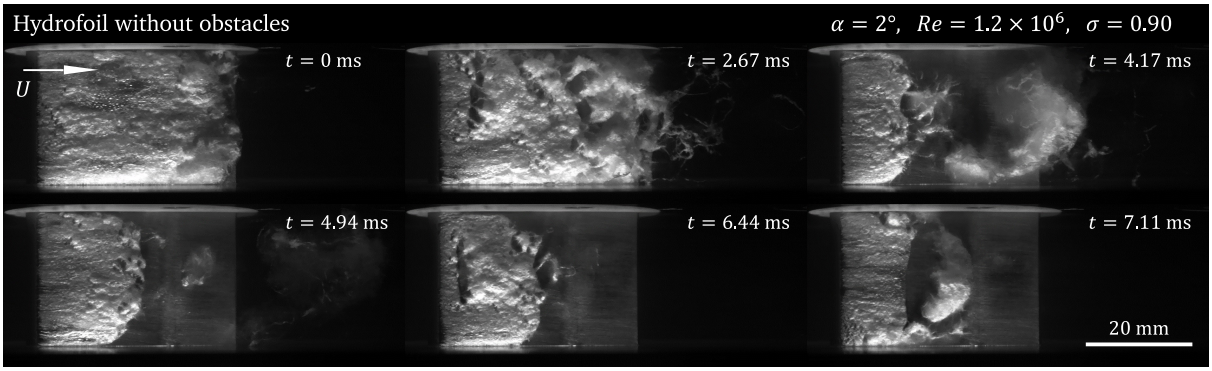

Figure 5: Series of high-speed images of cloud shedding for the hydrofoil without obstacles, at $\alpha = 2°$, $Re = 1.2 \times 10^6$ and $\sigma = 0.9$. The top row shows the sheet collapse and cloud separation of the main shockwave-driven shedding cycle, while the lower row displays the same stages for the secondary cycle.

For regime (ii), a strong influence on the frequencies corresponding to re-entrant flow-driven cloud cavitation is visible. In contrast to configuration (I) this influence is present for nearly the total range of cavitation numbers in the regime. This is due to the series of obstacles. With long sheet lengths, the re-entrant flow is already affected at an earlier stage. If it manages to overcome one obstacle, it is hindered by the next one. In addition, configuration (II) also leads to a greater reduction of the PSD of the characteristic frequencies. The difference is about 1 dB for the respective minimum. In figure 4 (c) an energy increase is visible in large parts of the sheet cavitation regime. This is most likely due to small, incoherent cavitation structures at each of the seven obstacles.

When the incidence angle is increased, the energy increase in the sheet cavitation regime is less recognisable. In regime (ii), the energy reduction of the frequencies corresponding to the re-entrant flow is less dominant at some points. As for hydrofoil configuration (I), this could be related to the thickness of the cavitation layer. The increase of the incidence angle leads to a reduced interaction of the shear layer and the obstacle close to the hydrofoil leading edge. This explains the quantitative reduction of the effects regarding shockwave-driven cloud shedding, as seen in regime (i) of figure 4 (d).

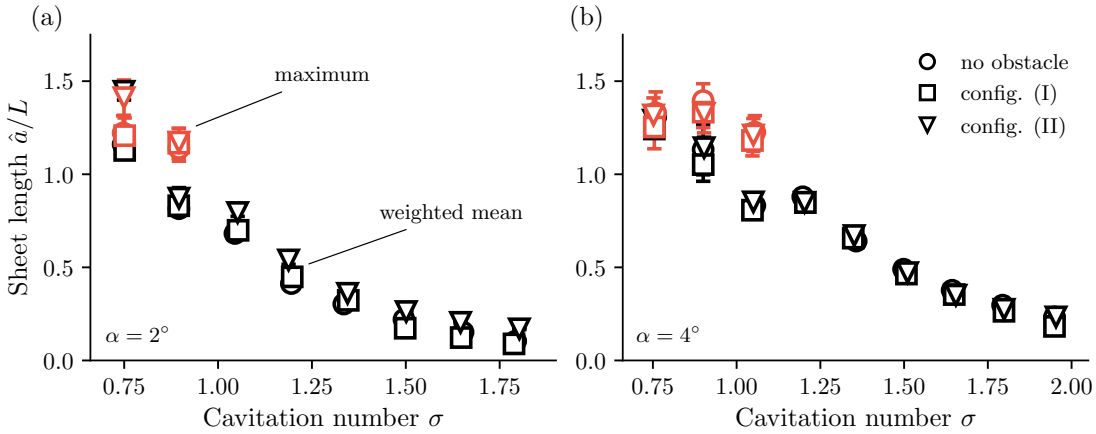

Figure 6: Comparison of the sheet lengths for the different hydrofoil configurations. Two methods are applied to determine the maximum and the weighted mean sheet length. The measurements were conducted at $Re = 1.2 \times 10^6$ and $\alpha = 2°$ (a) or $\alpha = 4°$ (b).

The results of the sheet length analysis are shown in figure 6. For both incidence angles, the well-known increase of the cavity sheet length by lowering the cavitation number is clearly visible. The 'weighted mean' method results in a small dip as the shockwave-driven cloud cavitation becomes the dominant shedding mechanism. The corresponding raw data of the sheet length for these operating points is very close to a normal distribution which causes the method to calculate the arithmetic mean value. The calculation of the maximum sheet length on the basis of shedding cycles (red markers in figure 6) is more suitable for these operating points with strong periodicity. However, it was not possible to use this method at higher cavitation numbers because the shedding cycles are no longer recognisable in the raw data. Once the cavitation number is further reduced ($\sigma < 0.9$) and the cavitation state is close to supercavitation, both methods match well. The comparison between the results of the different hydrofoil configurations shows a small increase in sheet length for the hydrofoil with multiple obstacles (II) at $\alpha = 2°$. The sheet length corresponding to hydrofoil configuration (I) and the hydrofoil without obstacles shows no significant differences. Once the incidence angle is increased to $\alpha = 4°$, there is almost no difference in sheet length between all configurations. Based on these results, it is plausible that the increase in sheet length for $\alpha = 2°$ and configuration (II) is caused by the influence of the first obstacle on the shear layer. As the angle of incidence increases, the height of the obstacle is no longer sufficient to influence the shear layer. A reduction of the sheet length, as indicated by other researchers [10, 11], could not be observed. Although the position of the obstacle in configuration (I) is very similar, the height of the obstacle in relation to the chord length is 25 % and 44.75 % smaller in the presented experiments compared to literature. Therefore, the single obstacle had no influence on the cavity sheet length.

5 Conclusion

The experimental results confirm that the re-entrant flow as a shedding mechanism can be stopped by the application of span-wise obstacles on the surface of a hydrofoil. In case of multiple obstacles that form a regular surface pattern, the blockage effect is strengthened. For operating points where shockwaves dominate the shedding process, the influence of the obstacles leads to a slight increase in the shedding frequency as secondary shedding cycles are suppressed. Further research is needed to explain the underlying mechanism. Apart from this observation, an influence of the surface pattern on the propagation of the shockwave could not be found. An obstacle at the leading edge of a hydrofoil, which influences the shear layer, causes the maximum cavity sheet length to increase. This growth in sheet length enables the transition from re-entrant flow to shockwave-driven cloud cavitation at higher cavitation numbers. Besides this, the application of the obstacles had no significant influence on the cavity sheet length. All observed effects are quantitatively reduced by an increase in incidence.

Acknowledgements

The results presented here were obtained as part of a research project no. 01IF 22710 N, funded by the Federal Ministry for Economic Affairs and Energy (BMWE) on the basis of a decision by the German Bundestag. The project work is conducted in collaboration with the Chair of Hydraulic Fluid Machinery at the Ruhr University Bochum.

References

[1] Brennen C E 1995 *Cavitation and bubble dynamics* (*Oxford engineering science series* vol 44) (New York: Oxford University Press)

[2] Dular M and Petkovšek M 2015 *Experimental Thermal and Fluid Science (EXP THERM FLUID SCI)* **68** 359–370 ISSN 0894-1777

[3] Hatzissawidis G, Kerres L, Ludwig G J and Pelz P F 2022 *IOP Conference Series: Earth and Environmental Science* **1079** 012046 URL https://dx.doi.org/10.1088/1755-1315/1079/1/012046

[4] Callenaere M, Franc J P, Michel J M and Riondet M 2001 *Journal of Fluid Mechanics* **444** 223–256 ISSN 0022-1120

[5] Ganesh H, Mäkiharju S A and Ceccio S L 2016 *Journal of Fluid Mechanics* **802** 37–78 ISSN 0022-1120

[6] Smith S M, Venning J A, Pearce B W, Young Y L and Brandner P A 2020 *Journal of Fluid Mechanics* **896** ISSN 0022-1120

[7] Hatzissawidis G, Kuhr M M and Pelz P F 2025 *Journal of Fluid Mechanics* **1004** A13

[8] Kawanami Y, Kato H, Yamaguchi H, Tanimura M and Tagaya Y 1997 *Journal of Fluids Engineering* **119** 788–794 ISSN 0098-2202

[9] Sato K, Tanada M, Monden S and Tsujimoto Y 2002 *JSME International Journal Series B* **45** 646–654 ISSN 1340-8054

[10] Zhang L, Chen M and Shao X 2018 *Ocean Engineering* **155** 1–9 ISSN 00298018

[11] Che B, Cao L, Chu N, Likhachev D and Wu D 2019 *Journal of Mechanical Science and Technology* **33** 4265–4279 ISSN 1738-494X

[12] Ganesh H 2015 *Bubbly Shock Propagation as a Cause of Sheet to Cloud Transition of Partial Cavitation and Stationary Cavitation Bubbles Forming on a Delta Wing Vortex* Ph.D. thesis University of Michigan

[13] Hatzissawidis G, Sieber M, Oberleithner K and Pelz P F 2025 *Experiments in Fluids* **66** 104 ISSN 1432-1114 URL https://doi.org/10.1007/s00348-024-03949-z